Journal of Applied Fluid Mechanics, Vol. 17, No. 5, pp. 967-979, 2024.
Available online at www.jafmonline.net, ISSN 1735-3572, EISSN 1735-3645.
https://doi.org/10.47176/jafm.17.05.2330

Examining the Influence of the Water Entry Velocity of Projectiles on Supercavity Flow and Ballistic Characteristics under Wave Conditions

J. Chen, H. Jia†, L. Zhang, Z. Wang and R. Xie

National-Provincial Joint Engineering Laboratory for Fluid Transmission System Technology, Zhejiang Sci-Tech University, Hangzhou 310018, China

†Corresponding Author Email: huixia.jia@zstu.edu.cn

ABSTRACT

In this study, we aim to examine the influence of water entry velocity of a single and two tandem projectile(s) on the supercavitation flow and projectile loading under wave conditions using numerical simulation. The volume of fluid model, renormalization group (RNG) κ-ε turbulence model, and Schnerr–Sauer cavitation model are adopted to simulate the multiphase, turbulent, and cavitation flow, respectively. The projectile movement is considered using overlapping grids and a six-degree-of-freedom model. The results show that as the projectile velocity increases, both the dimensionless maximum radius and length of the cavity, as well as the yaw angle, also increase with the rising water entry velocity. For the two tandem projectiles, the cavity pattern on the second projectile varies as the projectile velocity changes. With a lower projectile velocity, the second projectile cannot directly access the front cavity, and there may be situations wherein the part of the second projectile is not enveloped by cavity. As the projectile velocity increases, the second one can directly enter the cavity of the first projectile without forming a separate cavity around itself. In all of the examined cases, the peak pressure on the first projectile is approximately an order of magnitude higher than that on the second one. Furthermore, with increasing projectile velocity, the pressure peak ratio between the first and second projectiles increases.

Article History

Received September 26, 2023
Revised November 23, 2023
Accepted December 11, 2023
Available online February 24, 2024

Keywords:

Supercavitation
Wave model
Fluid dynamics
Multiple projectiles
Yaw angle

1. INTRODUCTION

The water entry problem is widely present in nature. It is known to play a significant role in defense and military fields, for example, in the application of antisubmarine missiles. Thus, the problem is a research hotspot in the field of fluid mechanics and has been under continuous investigation for over a hundred years.

Many studies have been dedicated to the water entry phenomenon of objects. For one, Worthington and Cole (1897) delved into vertical water entry experiments involving spheres, employing flash photography. Using meticulous photograph analysis, the authors dissected the attributes of splashing, the progressive closure of cavity surfaces, and other salient features emanating from the water entry of the sphere. Similarly, May and Woodhull (1948) performed vertical water experiments with spheres ranging in velocity from 7.9 m/s to 24.4 m/s. They established a correlation between the drag coefficient and Reynolds and Froude numbers. Extending their inquiry, they broadened the scope to encompass water entry trials encompassing an assortment of rotating bodies, such as cones and disks. This extension encompassed an investigation into the evolution of cavities, trajectories, drag coefficients during entry, and motion characteristics.

Advancements in high-speed imaging technology have propelled water entry experiments beyond conventional low speeds into the realm of higher velocities. For example, Honghui and Takami (2001) conducted pioneering water entry experiments involving projectiles, with an impressive water entry velocity of approximately 352 m/s. Based on their findings, they could establish a noteworthy correlation between the deflection of underwater projectile trajectories and the prevailing water depth. Furthermore, Yao et al. (2014) derived projectile motion equations that consider the negligible influence of gravity, coupled with a theoretical model delineating the evolutionary contours of cavity formations. Their investigations underscored the profound impact of cavity evolution on the stability of projectile trajectories. Moreover, Chen et al. (2019) have also examined the intricate interplay of projectile head

NOMENCLATURE

C_d	drag coefficient	$\bar{R}_{b,max}$	dimensionless maximum backflow-side cavity radius
D	projectile diameter	$\bar{R}_{y,max}$	dimensionless maximum upstream-side cavity radius
H	wave height	T	wave period
L	wave length	V	water-entry velocity
$\bar{L}_C$	dimensionless maximum cavity length	θ	yaw angle
Ma	Mach number		

morphology, incident angle, and impact velocity on high-speed water entry projectile stability. Their comprehensive exploration revealed that flat-headed projectiles exhibit heightened trajectory stability. However, an escalation in impact velocities and larger water entry angles were demonstrated to result in an augmented degree of trajectory instability.

In terms of numerical studies, Nguyen et al. (2013) conducted a study examining the supercavitating flow dynamics encountered via axisymmetric projectiles upon entry into water. Kamath et al. (2017) examined the progression of a freely descending wedge into water, meticulously documenting the evolution of the water jet and the changes in the free surface throughout the process.

Neaves and Edwards (2006) have also simulated the liquid water's compressibility using the Tait equation. This study explored the impact of water's compressibility on cavity evolution during the high-speed projectile water entry. Wang et al. (2017) investigated water compressibility's impact on supercavity evolution of subsonic, transonic, and supersonic projectiles. Remarkably, they proposed an approach to determine the supercavity contours within the cavitation number range from 10^{-3} to 10^{-5} for $0.276 < Ma < 2.2$.

For studies focusing on multiple projectiles entering water, numerical simulation method was primarily used. Jiang et al. (2021) performed numerical simulations to investigate the behavior of supersonic projectiles as they entered the water, examining both sequential and parallel entry scenarios. Their primary emphasis lies in examining the cavity's shape and its drag characteristics. As per their findings, in sequential water entry, the trailing projectile experiences lower impact drag as compared to the leading one. For parallel water entry, the cavity's inner boundary initially appears linear and then gradually transforms into an elliptical arc due to the plugging effect. Their research shed light on the hydrodynamics of multiple projectiles entering water and contribute to the understanding of cavity evolution and drag behavior. Moreover, Lu et al. (2022) performed numerical simulations involving high-speed projectiles entering water, exploring both synchronous and asynchronous parallel configurations. Their results indicate that, in asynchronous parallel entry, the trailing projectile experiences reduced impact loads compared with projectiles in synchronous parallel entry. This suggests that the timing difference between the entries of multiple projectiles can affect hydrodynamic interactions and impact loads during water entry.

The previously mentioned studies were carried out under the condition of tranquil water surface. However, waves, being the prevalent and paramount perturbations encountered on the ocean's surface, play a pivotal role in real-world scenarios.

Thus, Xiang et al. (2019) explored the effect of wave frequency and amplitude on a cylindrical body's water entry dynamics. Their research discovers a noteworthy phenomenon: the cylindrical body's trajectory experiences z-axis oscillations during water entry because of wave influence. The amplitude of the oscillation increases with the rise of wave amplitude and frequency.

In a study by Sun et al. (2019) investigating the vertical and inclined entry of a cone into a Stokes wave environment, they found that the pressure is asymmetric on the different sides of the cone surface due to the wave effect. Furthermore, the nonuniform distribution of the wave was identified as a key factor contributing to the nonlinearity observed in the vertical force. Their study unraveled the complicated impact of waves on the water entry behavior of a cone.

Similarly, Zhang et al. (2020) dedicated their research investigating the inclined water entry dynamics of a cylindrical body during regular wave environment, by employing a large eddy simulation method. Under regular wave conditions, the interaction among the cavity formation, deformation of water surface, and vortex patterns in the inclined water entry of a cylindrical body was examined.

Cheng et al. (2021) have also examined the mechanism of cavity formation for a semicircular float during inclined water entry under wave conditions. The results show that as wave nonlinearity increases, the asymmetry of the cavity shape becomes more pronounced. Moreover, Hu and Lui (2014) and Hu et al. (2017) established numerical wave models and conducted water entry simulations for flat-bottomed bodies and cylindrical bodies based on these models. Their findings demonstrated the relationship between impact force and wave height and wave period. Finally, Chen et al. (2022) investigated water entry dynamics for a three-dimensional full-scale wedge. They compared the differences of water entry between in calm waters and under wave influences.

In conclusion, the previous researches focus on the water-entry under still free surface conditions and the dynamics of single projectiles during the water-entry. The researches under wave conditions are relatively few. And the studies of the water-entry of successive projectiles under wave conditions is fewer. The research of the effect of the projectile velocity on the supercavitation and dynamics of successive projectiles under wave conditions could not be reported up to now.

In the paper, the effect of the projectile velocity on the supercavitation and dynamics of projectiles under wave conditions is studied. Under wave conditions, the influences of the projectile speed on the cavity contour and parameters, the impacting load of the projectile head and other dynamics parameters are analyzed and discussed.

2. NUMERICAL METHODS AND THEORETICAL MODEL

2.1 Governing Equations

For multiphase flow, this present study employs the volume of fluid model for computation. This method establishes the concept of the volume fraction α_q, defining the ratio of the volume filled within each fluid in a cell to the total cell volume. The volume fractions for liquid, gas, and water vapor are denoted as α_l, α_g, and α_v respectively, with their sum equating to 1. The governing equations encompass the continuity equation and momentum equation as follows:

$$\frac{\partial \rho_m}{\partial t}+\frac{\partial}{\partial x_i}(\rho_m u_i)=0 \tag{1}$$

$$\frac{\partial}{\partial t}(\rho_m u_i)+\frac{\partial}{\partial x_j}(\rho_m u_i u_j)=-\frac{\partial p}{\partial x_i}+ \frac{\partial}{\partial x_i}[(\mu_m+\mu_t)(\frac{\partial u_i}{\partial x_j}+\frac{\partial u_j}{\partial x_i}-\frac{2}{3}\frac{\partial \mu_k}{\partial x_k}\delta_{ij})]+S_M \tag{2}$$

where u_i and u_j represent velocity component in i and j direction; ρ_m stands for the mixed-phase density, $\rho_m = \sum \alpha_a \rho_a$; μ_m denotes the mixed-phase dynamic viscosity, $\mu_m = \sum \alpha_a \mu_a$; and S_M refers to the additional source term.

The turbulent model utilized in this study is the renormalization group (RNG) κ-ε model (Yakhot & Orszag, 1986). The turbulent kinetic energy equation and the dissipation rate equation are given by

$$\frac{\partial}{\partial t}(\rho_m \kappa)+\frac{\partial}{\partial x_i}(\rho_m u_i \kappa)=\frac{\partial}{\partial x_j}[\alpha_k(\mu_m+\mu_t)\frac{\partial \kappa}{\partial x_j}]+G_\kappa-\rho_m \varepsilon \tag{3}$$

$$\frac{\partial}{\partial t}(\rho_m \varepsilon)+\frac{\partial}{\partial x_i}(\rho_m u_i \varepsilon)=\frac{\partial}{\partial x_j}[\alpha_\varepsilon(\mu_m+\mu_t)\frac{\partial \varepsilon}{\partial x_j}]+ C_{1\varepsilon}G_\kappa\frac{\varepsilon}{\kappa}-C_{2\varepsilon}\rho_m\frac{\varepsilon^2}{\kappa} \tag{4}$$

where κ stands for turbulent kinetic energy; ε represents the dissipation rate; α_κ and α_ε are the Prandtl numbers for κ and ε, respectively; G_κ signifies the turbulent kinetic energy generated by velocity gradients; and $C_{1\varepsilon}$ and $C_{2\varepsilon}$ are empirical coefficients for turbulent kinetic energy dissipation rate, respectively.

The cavitation model used in this study is the Schnerr–Sauer model (Singhal et al., 2002), which is a homogeneous flow model based on the Rayleigh–Plesset bubble equation. It is known to trigger evaporation R_e from the liquid phase to the gas phase when the local pressure drops below the cavitation threshold. Conversely, it induces condensation R_c from the gas phase to the liquid phase when the local pressure exceeds the cavitation threshold. The transport equations are presented in the following manner:

$$\frac{\partial}{\partial t}(\alpha_v \rho_v)+\nabla\cdot(\alpha_v \rho_v u_v)=R_e-R_c \tag{5}$$

$$R_e=\frac{\rho_v \rho_l}{\rho_m}\alpha_v(1-\alpha_v)\frac{3}{R_B}\sqrt{\frac{2}{3}(\frac{p_v-p}{\rho_l})},\quad p\le p_v \tag{6}$$

$$R_c=\frac{\rho_v \rho_l}{\rho_m}\alpha_v(1-\alpha_v)\frac{3}{R_B}\sqrt{\frac{2}{3}(\frac{p-p_v}{\rho_l})},\quad p> p_v \tag{7}$$

where α_v represents the volume fraction of vapor, p_v represents the saturated vapor pressure, and R_B represents the bubble radius.

2.2 Wave Model

The velocity and volume fraction of the water at the inlet are defined to generate second-order Stokes waves (Dean & Dalrymple, 1991). To eliminate wave reflection at the computational domain boundaries, wave damping source terms are incorporated into the momentum equation. The Equations (8–9) show the velocity component of the second-order Stokes wave in the lateral and longitudinal direction, respectively, and the wave height is given in Equation (10).

$$u=\frac{\pi H}{T}\frac{\cosh(ky+kd)}{\sinh(kd)}\cos(kx-\omega t)+ \frac{3}{4}\frac{\pi H}{T}(\frac{\pi H}{L})\frac{\cosh(2ky+2kd)}{\sinh^4(kd)}\cos(2kx-2\omega t) \tag{8}$$

$$v=\frac{\pi H}{T}\frac{\sinh(ky+kd)}{\sinh(kd)}\sin(kx-\omega t)+ \frac{3}{4}\frac{\pi H}{T}(\frac{\pi H}{L})\frac{\sinh(2ky+2kd)}{\sinh^4(kd)}\sin(2kx-2\omega t) \tag{9}$$

$$\eta(x,t)=\frac{H}{2}\cos(kx-\omega t)+ \frac{H}{8}(\frac{\pi H}{L})\frac{\cosh(kd)}{\sinh^3(kd)}(\cosh(2kd)+2)\cos(2kx-2\omega t) \tag{10}$$

where T is the period, k is the wave number, L is the wave length, d is the water depth, and H is the wave height.

The wave damping zone in this study is established in the region equivalent to twice the wavelength ahead of the computational domain boundary. The damping term is given by

$$\frac{\partial u}{\partial t}+u\frac{\partial u}{\partial x}+v\frac{\partial u}{\partial y}=-\frac{1}{\rho}\frac{\partial p}{\partial x}+g_x+\nu(\frac{\partial^2 u}{\partial x^2}+\frac{\partial^2 u}{\partial y^2})-\beta u \tag{11}$$

$$\frac{\partial v}{\partial t}+u\frac{\partial v}{\partial x}+v\frac{\partial v}{\partial y}=-\frac{1}{\rho}\frac{\partial p}{\partial y}+g_y+\nu(\frac{\partial^2 v}{\partial x^2}+\frac{\partial^2 v}{\partial y^2})-\beta v \tag{12}$$

$$\beta(x)=\alpha\frac{(x-x_1)}{(x_2-x_1)},x_1\le x\le x_2 \tag{13}$$

where β is the wave damping coefficient; x_1 and x_2 represent the beginning and ending positions within the damping zone, respectively; and α is an empirical coefficient.

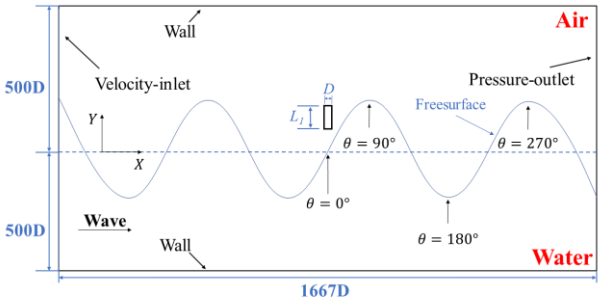

Fig. 1 Computational domain and boundary conditions

2.3 Numerical Model and Method

Figure 1 depicts the computational domain with dimensions of 1667*D* in length, 167*D* in width, and 1000*D* in height. The initial flow field is composed of an air domain with a height of 500*D* and a water domain with a height of 500*D*, sufficient to avoid boundary effects. The projectile is a cylinder with a diameter (*D*) of 6 mm and a length (L_1) of 48 mm. The weight of the projectile is 3.56 g, consisting of 5005 aluminum–magnesium alloy. The left boundary is assigned a velocity inlet boundary condition, whereas the right boundary assumes a pressure outlet boundary condition in the computational domain. The projectile wall and the remaining boundaries are configured as nonslip walls, which can be seen in Fig. 1. At the initial time, the projectile is located at a distance of one projectile length from the water surface and then moves downward along the negative direction of the y-axis.

The wave parameters used are as follows: wave length L = 2.2483 m and period T = 1.2 s. The wave propagates along the positive x-axis, while the projectiles move along the negative y-axis at the initial time. Figure 1 further clarifies wave phase definitions. The 90° wave phase corresponds to a wave crest, whereas the 270° wave phase corresponds to a wave trough.

The overlapping grid technology was used to handle the movement of projectiles in the computational domain. That is, two sets of mesh are adopted: one is the component mesh around a single projectile and the other is the background mesh for the whole computational domain. The parameters between the component mesh and background mesh are interchanged. The component- and background-mesh are given in Fig. 2, in which a two-dimensional locally enlarged view of the grid around the projectile is also provided. For both the background mesh and the component mesh, hexahedral grids are used. Moreover, the grids are refined near the free surface, the projectile, and its path.

2.4 Mesh Independence Test and Validation of Numerical Methods

Grid independence verification was conducted by establishing three sets of grids with different densities: 0.83 million cells (Case 1), 2.01 million cells (Case 2), and 2.98 million cells (Case 3). To verify grid independence,

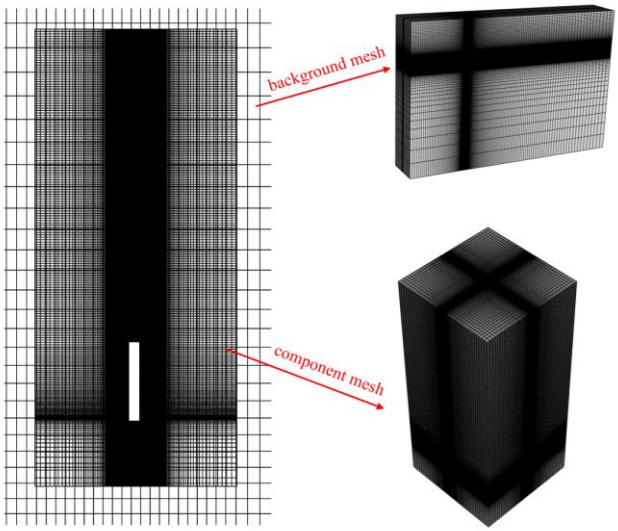

Fig. 2 The used computational mesh

simulations were conducted for a projectile with a velocity of 80 m/s entering the water at 0° phase.

Figure 3 shows the speed variation of the projectile with the time. Difference between Case 1 and Cases 2–3 can be observed, whereas the velocity variations for Case 2 and Case 3 grids are deemed similar. Thus, considering both computational accuracy and time constraints, we opted for the grid density identical to that of Case 2 in the subsequent numerical computations.

Validating the numerical methods involves two steps: first, validating the numerical wave flume; second, validating water entry for a projectile through numerical simulation.

The numerical wave flume model was based on the data from a previous study (Guo & Steen, 2011), and the parameters are as follows: length of 20 m, width of 1 m, height of 3.5 m, water depth of 3 m, and a damping zone length of 6 m. The parameters for the second-order Stokes

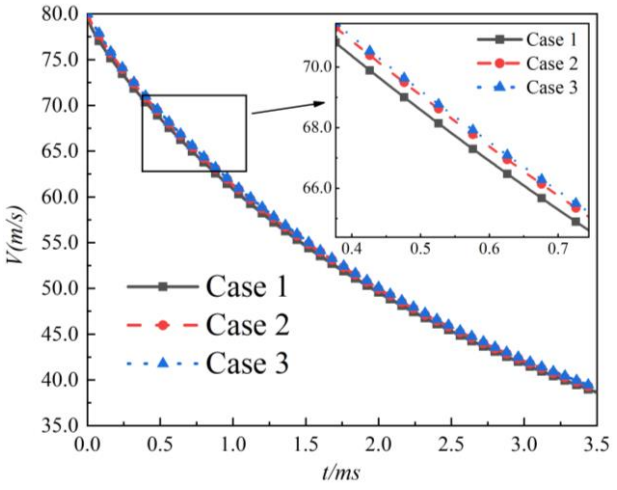

Fig. 3 Speed variation with the time for different mesh densities

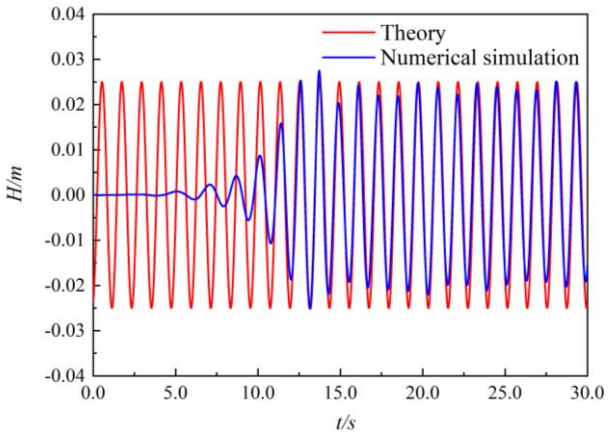

Fig. 4 Wave height variation with the time at a distance of 10 m

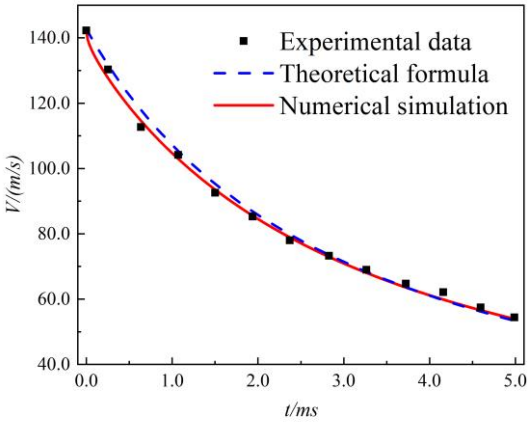

(a) Speed variation

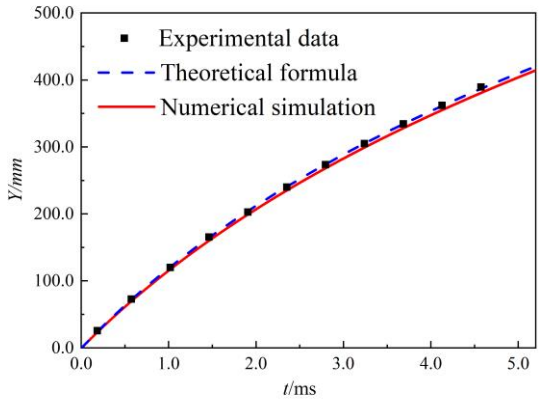

(b) Displacement variation

Fig. 5 Comparison of the variation of the speed and displacement among experimental data (Guo et al., 2012), numerical results and calculated values by theoretical analysis (Guo et al., 2012)

wave were as follows: wave height H = 0.05 m, wave length L = 2.2483 m, and period T = 1.2 s. We positioned a wave gauge 10 m in the wave propagation direction to monitor the wave height. The wave height variation with the time at this monitor location is presented in Fig. 4. The numerical simulation of the wave closely approximates the theory.

In validating the numerical simulations for high-speed projectile water entry, we utilized experimental data from a previous study (Guo et al., 2012). A three-dimensional numerical simulation was conducted. The dimensions of the simulated projectile were matched with those in the experiment: a cylindrical projectile with a diameter of 12.65 mm, length of 25.4 mm, and mass of 22.52 g. The projectile possesses an initial velocity of 142.7 m/s and has full freedom of movement along and rotation around all axes.

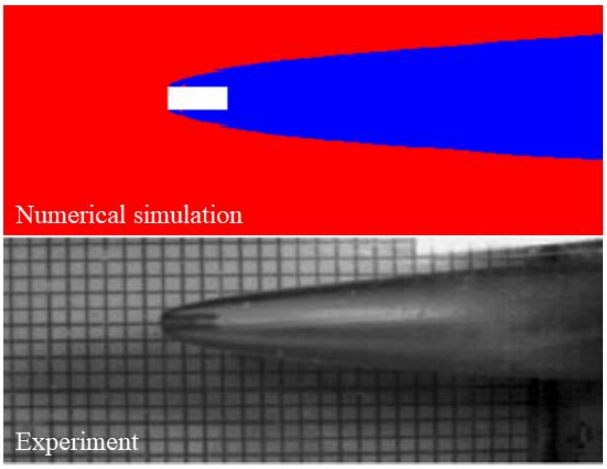

Fig. 6 Comparison of supercavitation profile between numerical simulation and experimental data (Guo et al., 2012)

Figures 5(a) and 5(b) depict the projectile's velocity and displacement changes after water entry, indicating strong agreement between numerical simulations, experimental data (Guo et al., 2012), and calculated values obtained through theoretical analysis (Guo et al., 2012). Figure 6 shows the cavity around the projectile in both numerical simulation and experimental results (Guo et al., 2012) at t = 3.0 ms, demonstrating strong alignment between the two.

3. RESULTS AND DISCUSSIONS

3.1 Water Entry of a Single Projectile Under Wave Condition

To explore the impact of velocity on the supercavity flow characteristics exhibited by a single projectile during its water entry in the presence of wave conditions, three different velocities were examined: V = 60 m/s, 80 m/s, and 100 m/s. For these three cases, the wave height H = 0.12 m and wave phase of 0° are the same. Figures 7(a)–(c) illustrate the supercavity evolution process after water entry for velocities of 60 m/s, 80 m/s, and 100 m/s, respectively. The moment the projectile first contacts the water is designated as t = 0 ms. In Fig. 7, there are diagrams of the water phase at time intervals of 0.4 ms between consecutive frames, covering the time span from 1.2 ms to 3.6 ms.

From Fig. 7, it is evident that differences of supercavitation exist when the projectile velocity is different. A higher entry velocity results in a slower cavity closure time and a delayed cavity collapse.

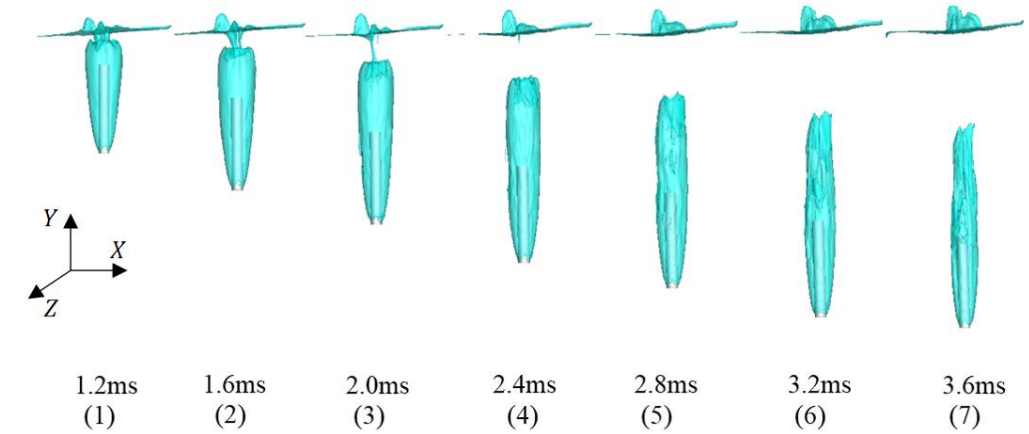

(a) V = 60 m/s

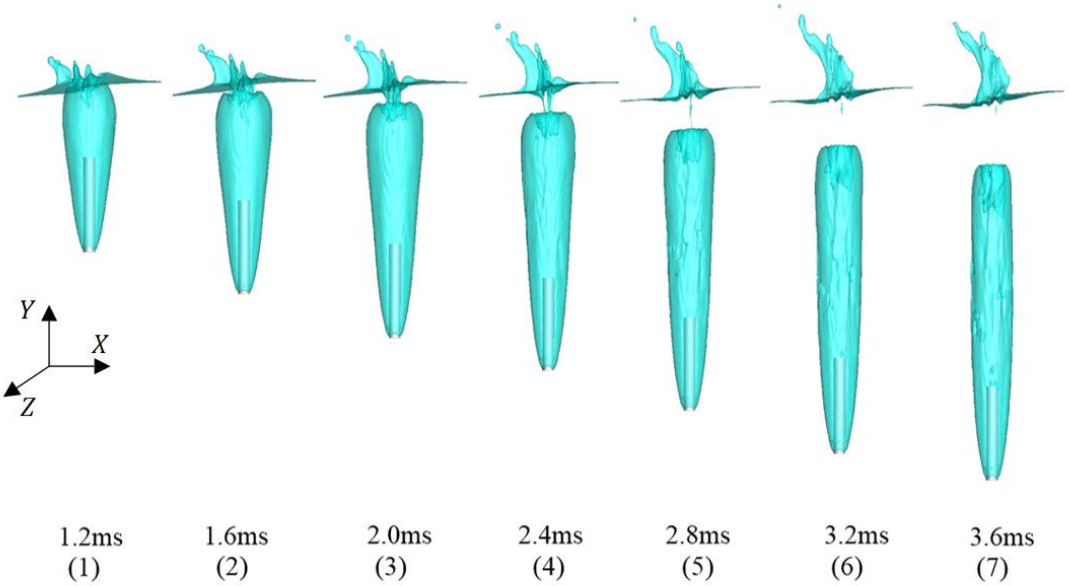

(b) V = 80 m/s

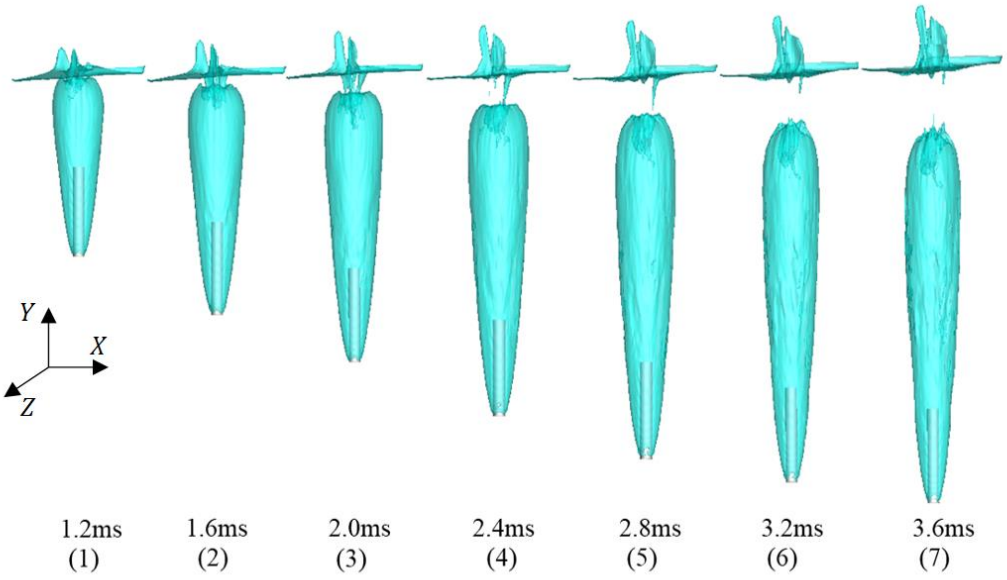

(c) V = 100 m/s

Fig. 7 Cavity evolution process for a single projectile entering water at different velocities under wave condition

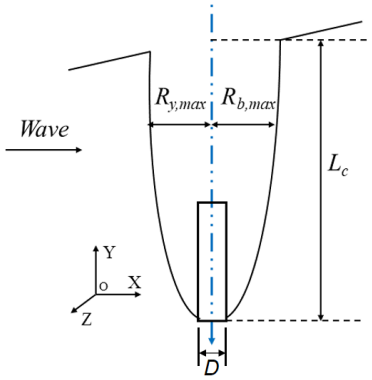

Fig. 8 Schematic diagram of cavity parameters with coordinate system

For the V = 60 m/s case, the cavity closes around t = 2.0 ms (Fig. 7(a)-3). At t = 2.8 ms (Fig. 7(a)-5), the collapse of the cavity was clearly observed at the tail. For the case of V = 80 m/s, the cavity closes around t = 2.4 ms (Fig. 7(b)-4). After cavity's closure, the cavity's tail remains relatively smooth (Fig. 7(b)-5). At t = 3.6 ms (Fig. 7(b)-7), the collapse of the cavity's tail is deemed evident. For the case of V = 100 m/s, the cavity also closes nearly at t = 2.4 ms (Fig. 7(c)-4). As time progresses, the cavity elongates with the projectile's descent. Moreover, the shape of supercavitation becomes slenderer, but the cavity collapse is unclear.

In addition, it can be seen that the water splash is different for the three cases. However, there is also the similarity: the water splash height on the left side exceeds that on the right side. This is due to the same 0° wave phase for the three velocities.

To comprehensively describe the cavity profile under wave conditions, several parameters are introduced to characterize the cavity shape. The definition schematic diagram is given in Fig. 8.

The side of the projectile that initially comes into contact with the wave is termed the upstream side, whereas the opposite side is referred to as the backflow side.

As shown in Fig. 8, L_C denotes the length of the supercavity, $R_{y,max}$ represents the maximum upstream cavity radius, and $R_{b,max}$ corresponds to the maximum backflow cavity radius.

To facilitate subsequent calculations and analysis, the abovementioned parameters have been nondimensionalized in this study, yielding dimensionless parameters, namely, dimensionless maximum cavity length $\bar{L}_C = L_C/D$; dimensionless maximum upstream-side cavity radius $\bar{R}_{y,max} = R_{y,max}/D$; and dimensionless maximum backflow-side cavity radius $\bar{R}_{b,max} = R_{b,max}/D$, where D is the projectile diameter.

Figure 9 shows the dimensionless maximum radius and length of the cavity on both the upstream and backflow sides under different velocity conditions.

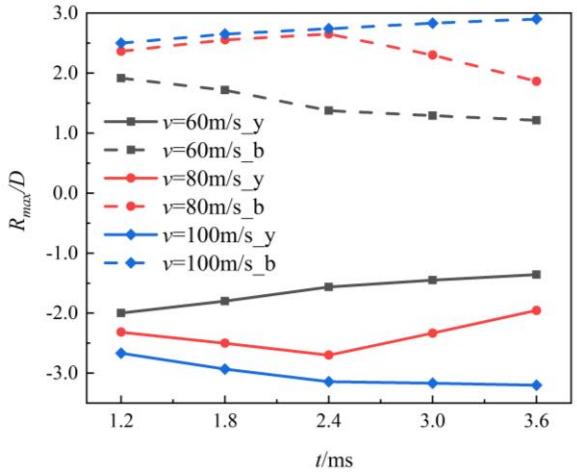

(a) Dimensionless maximum radius

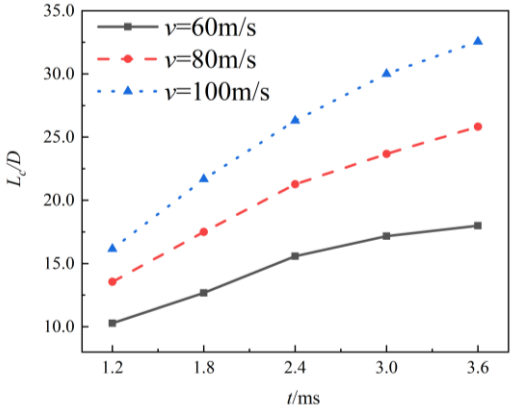

(b) Dimensionless length

Fig. 9 Dimensionless maximum radius and length on the upstream and backflow sides of the cavity for various water entry velocities

In Fig. 9(a), solid lines connect points that represent values on the upstream side, while dashed lines connect points that represent values on the backflow side.

It can be seen from Fig. 9(a) that at a certain time, an increased water entry velocity leads to a greater dimensionless maximum radius, both upstream and backflow sides of the cavity. Similarly, the cavity dimensionless length is larger with a higher projectile velocity, as shown in Fig. 9(b).

In addition, notably for V = 60 m/s, the cavity radius gradually decreases from t = 1.2 ms to 3.6 ms, whereas for V = 100 m/s, the cavity radius tends to slightly increase. For the case of V = 80 m/s, from t = 1.2 ms to 2.4 ms, the cavity radius slightly increases, while it decreases from t = 2.4 ms to 3.6 ms.

Furthermore, the dimensionless maximum radius of the supercavity on the upstream side exceeds that of the backflow side under all three conditions.

Throughout the projectile's water entry, the projectile experiences significant impact loads as it bumps with the water surface. In Fig. 10(a), a graph is shown depicting the temporal pressure variation at the projectile's head, with dimensionless pressure on the vertical axis and time on the horizontal axis.

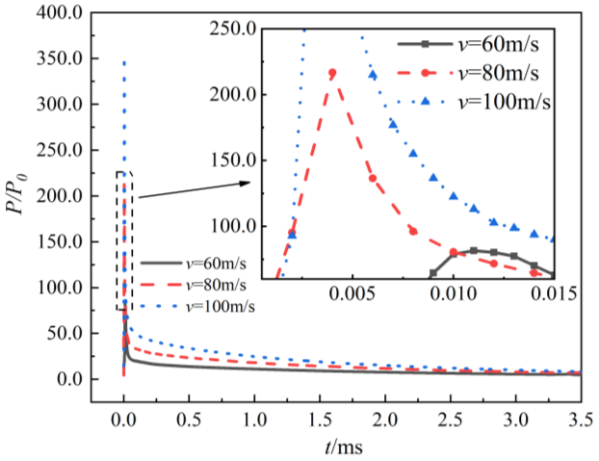

(a) Center point pressure

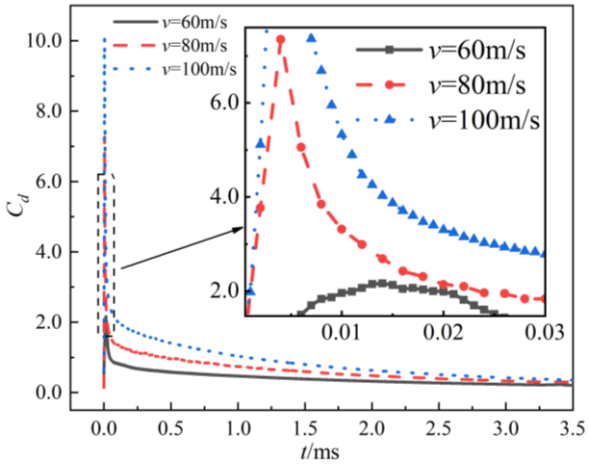

(b) Drag coefficient

Fig. 10 Time-varying curves of projectile loading

There is a huge sudden sharp peak observed for all three cases, as the projectile's head comes into contact with water.

As the projectile velocity elevates from 60 m/s to 80 m/s, the dimensionless pressure peak increases from approximately 80 to approximately 220, i.e., when the projectile velocity increases by approximately 33%, the pressure peak increases by approximately 175%.

As the projectile velocity elevates from 60 m/s to 100 m/s, the pressure peak increases from approximately 70 to 350, i.e., when the projectile velocity increases by approximately 70%, the pressure peak increases by approximately 400%.

Following the projectile impacting the free surface, the pressure rapidly decreases. The pressure on the head at a higher projectile velocity remains higher than that at lower projectile velocity.

In the research of Wang et al. (2020), they found that the pressure peak on the object's head increases with the grow of the water entry velocity. In addition, the pressure is up to its peak when the object's head touches the water surface, and then the peak rapidly decreases to be a quasi-constant value. The above findings are consistent with those in this article. It should be pointed out that the research of Wang et al. (2020) is under the condition of a quiescent water surface whereas the study here is under the condition with waves.

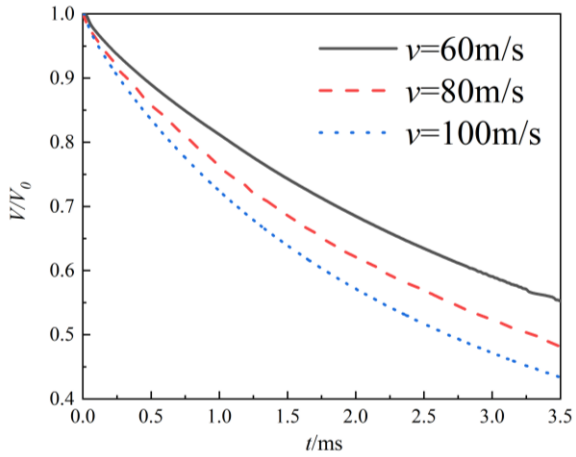

Fig. 11 Time-varying curves of projectile velocity

Figure 10(b) shows the time-dependent curve of the drag coefficient at various velocities, aligning with the pressure pattern: higher velocities correspond to higher drag coefficients. With the velocity increasing from 60 m/s to 100 m/s, the peak drag coefficient also rises by approximately 400%. The abovementioned conclusion is consistent with that in a previous study (Jiang et al., 2021).

Figure 11 depicts the velocity–time profiles of projectiles at different velocities. Coupled with Fig. 10(b), it is evident that higher entry velocities correspond to increased drag coefficients and intensified velocity decay rates. Over the course of a 3.5-ms interval, as the entry velocity progresses from 60 to 100 m/s, the resultant velocity attenuation undergoes magnitudes of 45.4%, 51.9%, and 57%, respectively.

Figures 12(a) and 12(b) depict the time-dependent curves of yaw angle and lateral displacement in the x-direction of the projectile at varying velocities. When the lateral displacement direction is the same with that along the wave propagation, the displacement value is deemed positive, and a positive yaw angle indicates counterclockwise rotation of the projectile around z-axis (Fig. 8). In Fig. 12(a), it is clear that a higher projectile motion velocity leads to a greater yaw angle. Moreover, there can be a pressure difference between the projectile's two sides that causes this.

From Fig. 12(b), under the same wave conditions, the projectile's lateral displacement increases with motion velocity. In the case of V = 100 m/s, the projectile initially shifts in the positive direction and then in the negative direction after cavity closure. For V = 60 m/s and 80 m/s, the lateral displacement is much smaller than that for V = 100 m/s.

3.2 Water Entry of Two Tandem Projectiles Under Wave Conditions

In this section, we explore how variations in water entry velocity affect the supercavity flow characteristics of

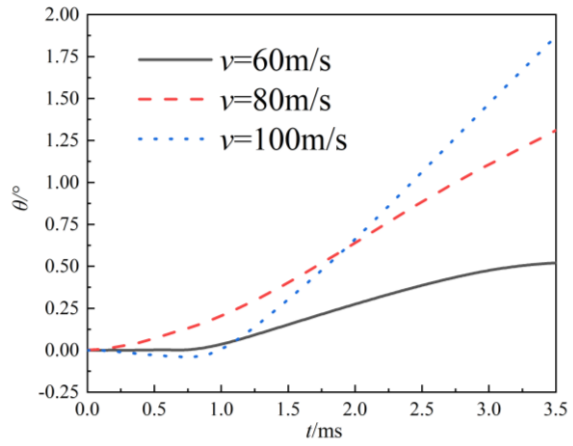

(a) Yaw angle

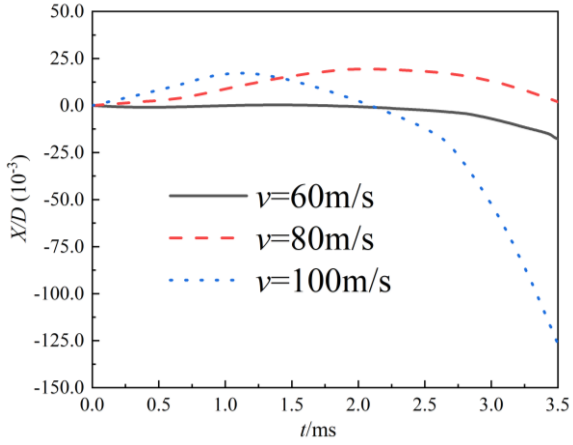

(b) Lateral displacement

Fig. 12 Time-varying curves of yaw angle and lateral displacement for the projectile

multiple projectiles under wave conditions. Similar to the research of single projectile, three water entry velocities have been selected, namely, V = 60 m/s, 80 m/s, and 100 m/s. Similarly, except for the projectile velocity, the wave phase and wave height remain consistent across different conditions, i.e., the wave height is 0.12 m with wave phase set at 0°. The spacing between two projectiles is 20D.

As shown in Fig. 13, the supercavity evolution of two tandem projectiles in the course of water entry is given.

From Fig. 13(a)–(c), it can be observed that during t = 0.8 ms to 1.4 ms, an open cavity forms for the first projectile, while the second one remains airborne for all three conditions. At t = 2.0 ms, for V = 60 m/s, the second projectile remains to be airborne, whereas for V = 80 m/s, its second projectile has started to interact with the disturbed surface. In addition, at t = 2.0 ms for V = 100 m/s, the following projectile enters the cavity generated via the first projectile.

At t = 3.2 ms, for V = 60 m/s, the cavity of the first projectile has already closed before the second projectile enters it. However, for V = 80 m/s and 100 m/s, the following projectile is already inside the cavity simultaneously.

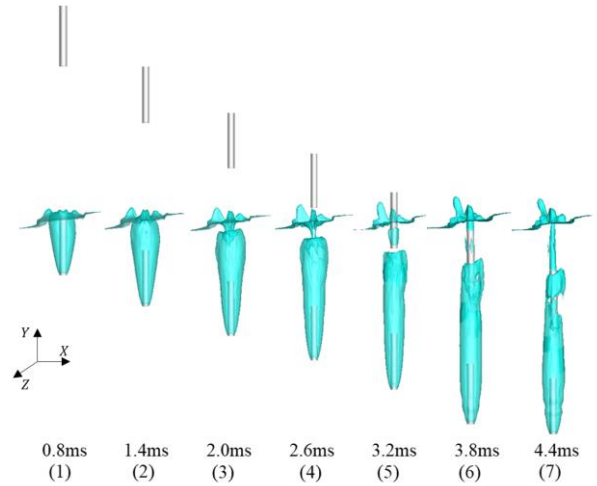

(a) V = 60 m/s

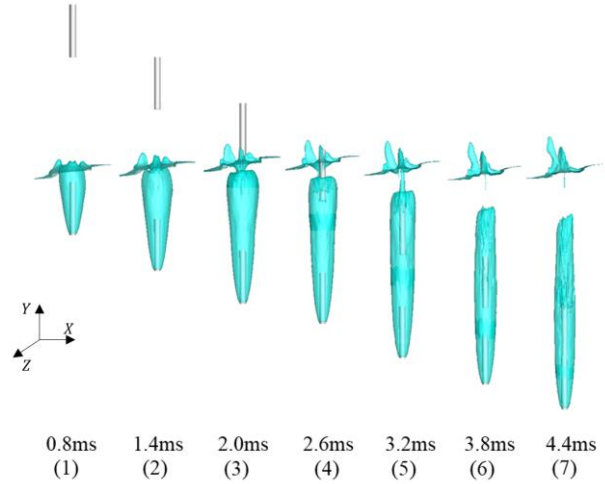

(b) V = 80 m/s

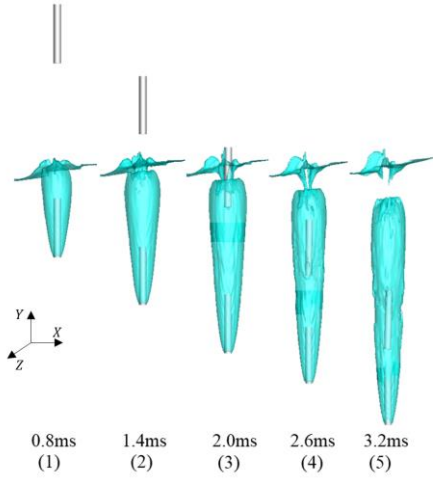

(c) V = 100 m/s

Fig. 13 Supercavity evolution of two tandem projectiles entering water under wave conditions

At t = 4.4 ms, for V = 60 m/s, the cavity collapses and cannot fully envelop the following projectile. For V = 80 m/s, the following projectile completely enters the front cavity and will then collide with the first one. As for V = 100 m/s, the following projectile has collided with the first one, which is beyond the scope of the study and thus will not be discussed here.

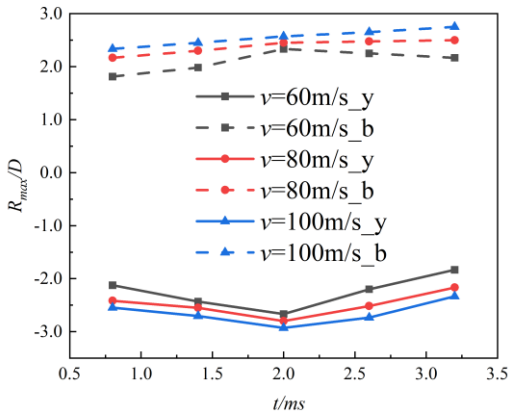

Fig. 14 Dimensionless maximum radius on the upstream and backflow sides of the cavity

Furthermore, it can be seen that for V = 80 m/s and 100 m/s, the following projectile enters the front cavity passing through the disturbed free surface, whereas for V = 60 m/s, the head of the second projectile at t = 3.2 ms did not enter the front cavity; thus, no complete cavity was formed around the second projectile to encase it. Thus, the second projectile made direct contact with water. This phenomenon did not occur under the other two conditions.

Figure 14 shows the dimensionless maximum radius on the upstream and backflow sides of the cavity under various scenarios. As observed in Fig. 14, from t = 0.8 ms to 3.2 ms, higher projectile velocities lead to larger maximum cavity radius.

In Fig. 15, the pressure variation curves at the second projectile head's center point and the drag coefficient over time for different water entry velocities in the presence of wave conditions are presented. The change in pressure and drag coefficient at the first projectile's head center mirrors that of the single projectile and is not given here again. When necessary, reference is made to the single projectile results (as seen in Fig. 10).

Figure 15(a) depicts that the pressure of the second projectile's head center point in all three cases first rises to a peak and then rapidly decreases, which is similar to that for the first or single projectile. However, there are also some differences. First, the second projectile experiences significantly lower peak pressures as compared to the first one for all three cases.

With a water entry velocity of 60 m/s, the dimensionless pressure peak on the second projectile measures approximately 19, whereas the value reaches approximately 110 for the first projectile.

At a water entry velocity of 80 m/s, the dimensionless pressure peak on the second projectile is approximately 23, whereas it is approximately 170 for the first projectile.

When the water entry velocity is increased to 100 m/s, the dimensionless pressure peak on the first and second projectile is approximately 320 and 33, respectively; i.e., when the water entry velocity changes from 60 m/s, 80 m/s, to 100 m/s, the peak pressure on the head of the second

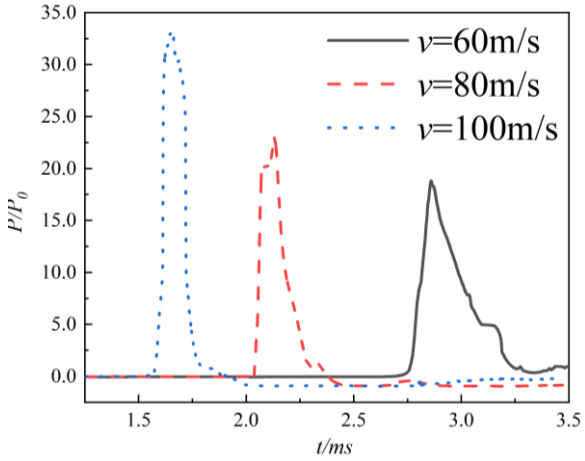

(a) Center point pressure

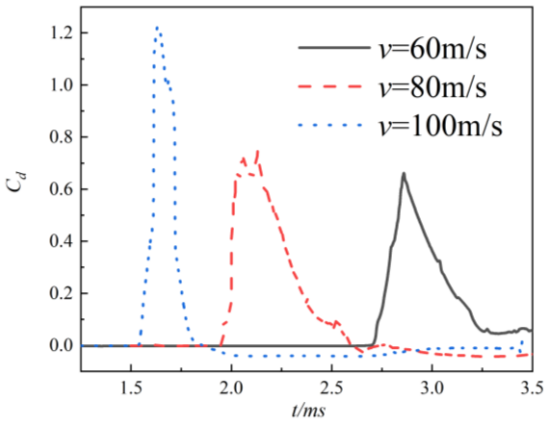

(b) Drag coefficient

Fig. 15 Load change on the second projectile

projectile as compared with that of the first projectile is reduced by approximately 83%, 87%, and 90%, respectively.

The second difference of the pressure at the head between the first and second projectiles is that the interval between the rapid pressure increase and decrease at the second projectile's head is longer as compared to the first projectile. For the first projectile, the required time for this process is almost 0 ms, whereas for the second projectile, it takes approximately 0.5, 0.3, and 0.2 ms, with the water entry velocity of 60 m/s, 80 m/s, and 100 m/s.

In addition, the timing of the peak pressure at the second projectile's head vary, which is caused by the different velocities of the second projectile.

Figure 15(b) shows that the variation trend of the drag coefficient is consistent with the pressure change at the projectile's head for all three cases.

The peak value of the drag coefficient on the second projectile is approximately 0.65, 0.75, and 1.25, respectively, with water entry velocity of 60 m/s, 80 m/s, and 100 m/s; moreover, on the first projectile, it is 3.5, 6.0, and 9.0, respectively.

That is, the drag coefficient's peak value for the second projectile is considerably less than the peak value

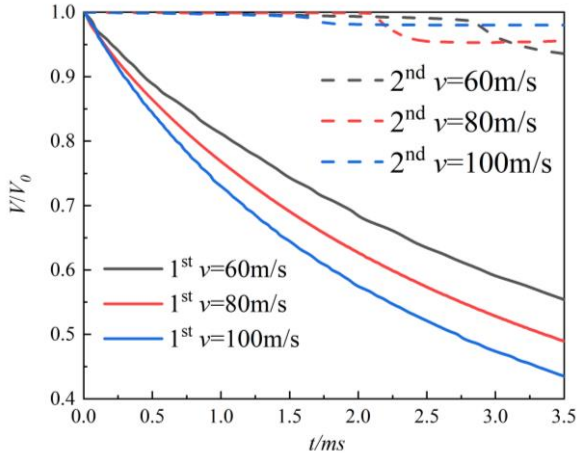

Fig. 16 Velocity change with time for the first and second projectiles

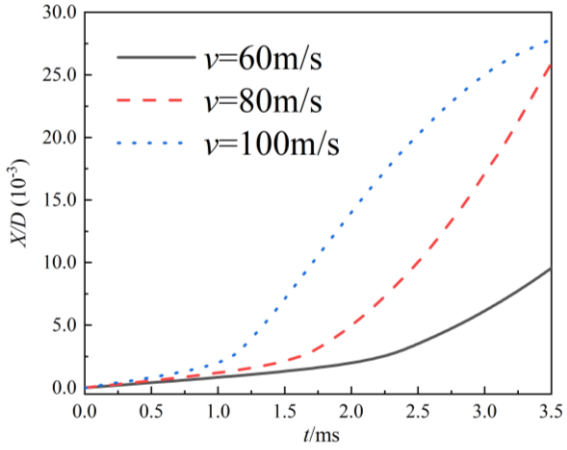

Fig. 17 Lateral displacement change of the first projectile with time

observed on the first projectile in all cases. The peak value of the drag coefficient on the second projectile can be reduced by approximately 81%–88% for the three cases compared with that on the first one. In a study by Jiang et al. (2021), approximately 80% reduction of the drag coefficient on the second cylinder is observed as compared to that of the first one, which is consistent with the findings of this present study.

Comparing the pressure and drag coefficient between the first and second projectiles, it becomes evident that both the drag coefficient on the second projectile and the peak pressure at the second projectile's head center are notably lower than their counterparts on the first projectile. This means that the disturbed free surface is helpful in reducing the projectile loading.

Figure 16 illustrates the variation in velocity for both the first and second projectiles at different entry speeds. Compared with the result of a singular projectile, it is evident that the second projectile has a negligible impact on the velocity decay of the first projectile. Conversely, for the second projectile, higher initial velocities induce earlier interactions with the disturbed water surface generated by the first projectile, leading to an earlier beginning of velocity attenuation. Moreover, the rate of velocity decay for the second projectile is notably reduced as compared to that of the first projectile.

Figure 17 depicts the lateral displacement change of the first projectiles with time.

It can be seen that the lateral displacements of the projectiles are very small for the three cases despite considering the influence of waves. It appears that the lateral displacement of the first projectile increases with the rising water entry velocity.

For the second projectile, the lateral displacement change with time is in the same order of magnitude of that of the first projectile (no figure). Similarly, the lateral displacement of the second projectile increases with the rising water entry velocity.

Figure 18 presents the time evolution of yaw angles for the second projectile. The positive value means that the

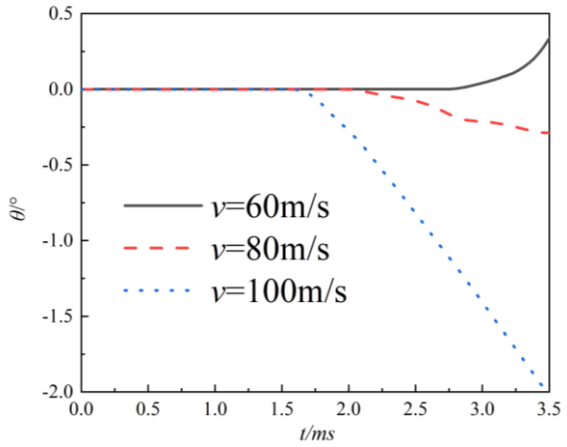

Fig. 18 Yaw angle change of the second projectile with time

projectile rotates counterclockwise. As shown in Figure 18, the yaw angle of the second projectile is more pronounced with higher projectile velocities. The yaw angle of the second projectile is less than 0.5° for the case of 60 m/s and 80 m/s. However, the value is approximately 2° under the case of water entry velocity 100 m/s, and the 2° yaw angle is sufficient to be directly observed in Fig. 13. Moreover, the yaw angles of the first projectile for the three cases are deemed very small, i.e., less than 1° (no figure), and will not be discussed further.

It can also be seen that the time at which the magnitude of the yaw angle increases is different for three cases. This is due to the different times when the head of the second projectile interacts with the disturbed water splashes.

4. CONCLUSIONS

In this study, the flow field of the water-entry of a single projectile and tandem projectiles under wave conditions are simulated. The effects of the water-entry velocity on the cavity contour and parameters, the impacting load of the projectile head and other dynamics

parameters under wave conditions are analyzed. The conclusions obtained are as follows:

(1) When projectiles enter the water under wave conditions at varying speeds, the time of cavity collapse delays with increasing projectile velocity. Furthermore, as velocity rises, the dimensionless maximum radius and cavity length increase.

(2) The pressure peak at the projectile head center rises with increasing projectile velocity. In the examined cases, when the projectile velocity increases by approximately 67%, both the pressure peak and drag coefficient increase by approximately four times. The presence of waves leads to an asymmetry on both sides of the projectile, and as velocity rises, so does the yaw angle.

(3) For the two tandem projectiles, with variations in water entry velocity, the cavity pattern on the second projectile is different. With lower projectile velocity, the second projectile cannot directly enter the front cavity, potentially resulting in situations where a portion of it remains outside the cavity. As the projectile velocity increases, the second projectile can enter the first projectile's cavity directly without forming a separate cavity around itself.

(4) In all the examined cases, the peak pressure on the first projectile is significantly higher, approximately one order of magnitude above that on the second projectile. In addition, the pressure peak ratio between the first and second projectiles increases with the increasing projectile velocity.

ACKNOWLEDGEMENTS

This research was funded by the Natural Science Foundation of Zhejiang Province, China (grant number: LQ13A020005, LY17E060006) and National Natural Science Foundation of China (grant number: 51876194, 52176048, U1909216).

CONFLICT OF INTEREST

The authors declare no conflict of interest.

AUTHORS CONTRIBUTION

Conceptualization: **H. X. Jia** and **L. T. Zhang**. Methodology: **H. X. Jia**. Investigation**: J. W. Chen** and **R. S. Xie**. Validation: **J. W. Chen**. Formal analysis: **J. W. Chen** and **Z. K. Wang**. Writing–original draft: **J. W. Chen**. Writing–review and editing: **H. X. Jia**. Visualization: **J. W. Che**n. Supervision: **L. T. Zhang**. Project administration: **L. T. Zhang**.

REFERENCES

Chen, J., Xiao, T., Wu, B., Wang, F., & Tong, M. (2022). Numerical study of wave effect on water entry of a three-dimensional symmetric wedge. *Ocean Engineering, 250,* 110800. https://doi.org/10.1016/j.oceaneng.2022.110800

Chen, T., Huang, W., Zhang, W., Qi, Y., & Guo, Z. (2019). Experimental investigation on trajectory stability of high-speed water entry projectiles. *Ocean Engineering, 175,* 16-24. https://doi.org/10.1016/j.oceaneng.2019.02.021

Cheng, Y., Yuan, D., & Ji, C. (2021). Water entry of a floating body into waves with air cavity effect. *Journal of Fluids and Structures, 104,* 103302. https://doi.org/10.1016/j.jfluidstructs.2021.103302

Dean, R. G., & Dalrymple, R. A. (1991). *Water wave mechanics for engineers and scientists* (Vol. 2). World Scientific Publishing Company.

Guo, B., & Steen, S. (2011, January). *Comparison of numerical methods for wave generation by VOF-based numerical wave tank.* International Conference on Offshore Mechanics and Arctic. https://doi.org/10.1115/OMAE2011-49777

Guo, Z., Zhang, W., Xiao, X., Wei, G., & Ren, P. (2012). An investigation into horizontal water entry behaviors of projectiles with different nose shapes. *International Journal of Impact Engineering, 49,* 43-60. https://doi.org/10.1016/j.ijimpeng.2012.04.004

Honghui, S., & Takami, T. (2001). Hydrodynamic behavior of an underwater moving body after water entry. *Acta Mechanica Sinica, 17*(1), 35-44. https://doi.org/10.1007/BF02487768

Hu, X., & Liu, S. (2014). Numerical investigation of wave slamming of flat bottom body during water entry process. *Mathematical Problems in Engineering*, *2014*. https://doi.org/10.1155/2014/821689

Hu, X., Jiang, Y., & Cai, D. (2017). Numerical modeling and simulation of wave impact of a circular cylinder during the submergence process. *Modelling and Simulation in Engineering, 2017*. https://doi.org/10.1155/2017/2197150

Jiang, Y., Li, Y., Guo, J., Yang, L., & Wang, H. (2021). Numerical simulations of series and parallel water entry of supersonic projectiles in compressible flow. *Ocean Engineering, 235,* 109155. https://doi.org/10.1016/j.oceaneng.2021.109155

Kamath, A., Bihs, H., & Arntsen, Ø. A. (2017). Study of water impact and entry of a free falling wedge using computational fluid dynamics simulations. *Journal of Offshore Mechanics and Arctic Engineering, 139*(3), 031802. https://doi.org/10.1115/1.4035384

Lu, L., Yan, X., Li, Q., Wang, C., & Shen, K. (2022). Numerical study on the water-entry of asynchronous parallel projectiles at a high vertical entry speed. *Ocean Engineering, 250*, 111026. https://doi.org/10.1016/j.oceaneng.2022.111026

May, A., & Woodhull, J. C. (1948). Drag coefficients of steel spheres entering water vertically. *Journal of Applied Physics, 19*(12), 1109-1121. https://doi.org/10.1063/1.1715027

Neaves, M. D., & Edwards, J. R. (2006). All-speed timeaccurate underwater projectile calculations using

a preconditioning algorithm. Journal of Fluids *Engineering*, 128(2), 284-296.

Nguyen, V. T., Ha, C. T., & Park, W. G. (2013, November). *Multiphase flow simulation of water-entry and-exit of axisymmetric bodies.* ASME International Mechanical Engineering Congress and Exposition. American Society of Mechanical Engineers. https://doi.org/10.1115/IMECE2013-64691

Singhal, A. K., Athavale, M. M., Li, H., & Jiang, Y. (2002). Mathematical basis and validation of the full cavitation model. *Journal of Fluids Engineering, 124*(3), 617-624. https://doi.org/10.1115/1.1486223

Sun, S. L., Liu, B. W., & Zhang, A. M. (2019). On the fully nonlinear water entry of a cone in Stokes wave. *Engineering Analysis with Boundary Elements, 98,* 232-242. https://doi.org/10.1016/j.enganabound.2018.10.019

Wang, C., Wang, G., Zhang, M., Huang, B., & Gao, D. (2017). Numerical simulation of ultra-high speed supercavitating flows considering the effects of the water compressibility. *Ocean Engineering, 142*, 532-540. https://doi.org/10.1016/j.oceaneng.2017.07.041

Wang, Y., Ye, B., Wang, Z., Huang, J., Wang, Y., & Huang, C. (2020). Vertical water entry of projectiles with surface seal. *Ocean Engineering, 216*, 107606. https://doi.org/10.1016/j.oceaneng.2020.107606

Worthington, A. M., & Cole, R. S. (1897). V. Impact with a liquid surface, studied by the aid of instantaneous photography. *Philosophical Transactions of the Royal Society of London. Series A, Containing Papers of a Mathematical or Physical Character, (189),* 137-148. https://doi.org/10.1098/rsta.1897.0 005

Xiang, G., Li, X., Yu, X., Luo, Y., & Cao, Y. (2019). Motion dynamics of dropped cylindrical objects in flows after water entry. *Ocean Engineering, 173*, 659-671. https://doi.org/10.1016/j.oceaneng.2019.01.010

Yakhot, V., & Orszag, S. A. (1986). Renormalization group analysis of turbulence. I. Basic theory. *Journal of Scientific Computing, 1*(1), 3-51. https://doi.org/10.1007/BF01061452

Yao, E., Wang, H. R., Pan, L., Wang, X. B., & Woding, R. H. (2014). Vertical water-entry of bullet-shaped projectiles. *Journal of Applied Mathematics and Physics, 2*(06), 323. http://dx.doi.org/10.4236/jamp.2014.26039

Zhang, G. Y., Hou, Z., Sun, T. Z., Wei, H. P., Li, N., Zhou, B., & Gao, Y. J. (2020). Numerical simulation of the effect of waves on cavity dynamics for oblique water entry of a cylinder. *Journal of Hydrodynamics, 32,* 1178-1190. https://doi.org/10.1007/s42241-020-0083-4